Upper mantle seismic structure beneath central East Antarctica from body wave tomography: Implications for the origin of the Gamburtsev Subglacial Mountains.

Andrew J. Lloyd

Department of Geosciences, Pennsylvania State University, University Park, Pennsylvania, USA

Department of Earth and Planetary Sciences, Washington University in St. Louis, St. Louis, Missouri, USA (a.j.lloyd@go.wustl.edu)

Andrew A. Nyblade

Department of Geosciences, Pennsylvania State University, University Park, Pennsylvania, USA

Douglas A. Wiens and Patrick J. Shore

Department of Earth and Planetary Sciences, Washington University in St. Louis, St. Louis, Missouri, USA

Samantha E. Hansen

Department of Geological Sciences, University of Alabama, Tuscaloosa, Alabama, USA

Masaki Kanao

Geoscience Research Group and Polar Data Center, National Institute of Polar Research, Tokyo, Japan

Dapeng Zhao

Department of Geophysics, Tohoku University, Sendai, Japan

[1] The Gamburtsev Subglacial Mountains (GSM), located near the center of East Antarctica, are the highest feature within the East Antarctic highlands and have been investigated seismically for the first time during the 2007/2008 International Polar Year by the Gamburtsev Mountains Seismic Experiment. Using data from a network of 26 broadband seismic stations and body wave tomography, the P and S wave velocity structure of the upper mantle beneath the GSM and adjacent regions has been examined. Tomographic images produced from teleseismic P and S phases reveal several large-scale, small amplitude anomalies ($\delta V_p = 1.0\%$, $\delta V_s = 2.0\%$) in the upper 250 km of the mantle. The lateral distributions of these large-scale anomalies are similar in both the P and S wave velocity models and resolution tests show that they are well resolved. Velocity anomalies indicate slower, thinner lithosphere beneath the likely Meso- or Neoproterozoic Polar Subglacial Basin and faster, thicker lithosphere beneath the likely Archean/ Paleoproterozoic East Antarctic highlands. Within the region of faster, thicker lithosphere, a lower amplitude ($\delta V_p = 0.5\%$, $\delta V_s = 1.0\%$) slow to fast velocity pattern is observed beneath the western flank of the GSM, suggesting a suture between two lithospheric blocks possibly of similar age. These findings point to a Precambrian origin for the high topography of the GSM, corroborating other studies invoking a long-lived highland landscape in central East Antarctica, as opposed to uplift caused by Permian/Cretaceous rifting or Cenozoic magmatism. The longevity of the GSM makes them geologically unusual; however, plausible analogs exist, such as the 550 Ma Petermann Ranges in central Australia. Additional uplift may

have occurred by the reactivation of pre-existing faults, for example, during the Carboniferous-Permian collision of Gondwana and Laurussia.

1. Introduction

[2] The Gamburtsev Subglacial Mountains (GSM) are located near the center of East Antarctica, reaching elevations of ~3 km with relief on the order of 1–2 km that is characterized by classic alpine geomorphology (Figures 1 and 2) [*Bo et al.*, 2009; *Ferraccioli et al.*, 2011]. The 2–3 km thick East Antarctic ice sheet obscures the geology and tectonic structure of the GSM and precludes the collection of geologic samples. Therefore, with only reconnaissance-scale geophysics, it has been difficult to determine the origin of the high and rugged topography.

[3] Tectonic reconstructions of East Antarctica and geochemical studies of the interior based on U-Pb ages from detrital zircons, as well as $^{40}Ar/^{39}Ar$ ages from detrital hornblends suggest that the last major tectonic event in the East Antarctic interior was prior to 480 Ma [*van del Flierdt et al.*, 2008; *Veevers and Saeed*, 2011], leading some to suggest the GSM could be a remnant of the Australian Pinjarra Orogeny [*Fitzsimons*, 2003] or formed through a series of ancient collisional orogenies spanning from 1.0 to 0.5 Ga [*Veevers and Saeed*, 2008]. More recent uplift may have been accomplished by crustal shortening during the Variscan collision of Gondwana and Laurussia [Veevers, 1994], Permian convergence along the Paleo-Pacific margin of East Antarctica [*Lisker et al.*, 2003], or by a combination of erosional unloading, Permian and Cretaceous rift flank uplift of a postulated East Antarctic rift system, and warming of the crustal root beneath the GSM [*Phillips and Läufer*, 2009; *Ferraccioli et al.*, 2011]. Alternatively, *Sleep* [2006] notes that thinner lithosphere (~150–220 km) in the vicinity of the GSM [*Morelli and Danesi*, 2004] is characteristic of Cenozoic magmatism and suggests that the GSM

represents a young hotspot orogeny, similar to the Hoggar Massif in the central Sahara.

[4] In this study, we use *P* and *S* wave travel time residuals from teleseismic events recorded by the Gamburtsev Mountains Seismic Experiment (GAMSEIS) to produce tomographic images of the upper mantle velocity structure beneath the GSM and adjoining regions of East Antarctica. The results provide new constraints on both the origin of the GSM and the tectonic framework of central East Antarctica. Following a brief review of the tectonic history and past geophysical studies of the East Antarctic lithosphere, we present the data and methods used in the tomographic inversions along with the resulting *P* and *S* wave velocity models, and then in the final section we discuss the implications of the tomographic images for the tectonic framework of central East Antarctica and the origin of the GSM.

2. Background

2.1. Tectonic History of East Antarctica

[5] Little is known of the geology and tectonic history of East Antarctica due to the 2–3 km thick East Antarctic ice sheet that obscures all but a handful of outcrops along the coast and in the Transantarctic Mountains (TAM; Figure 1). *In situ* geologic studies indicate that Archean to Proterozoic outcrops prevail along the East Antarctic coast [*Tingey*, 1991] and Proterozoic outcrops are seen throughout the Transantarctic Mountains [*Goodge et al.*, 2001]. Most tectonic reconstructions have therefore assumed that East Antarctica is a Precambrian shield with an Archean nucleus that formed prior to or during the amalgamation of Rodinia [*Dalziel*, 1991; *Hoffman*, 1991; *Moores*, 1991; *Tingey*, 1991; *Rogers et al.*, 1995], while others have suggested that the final
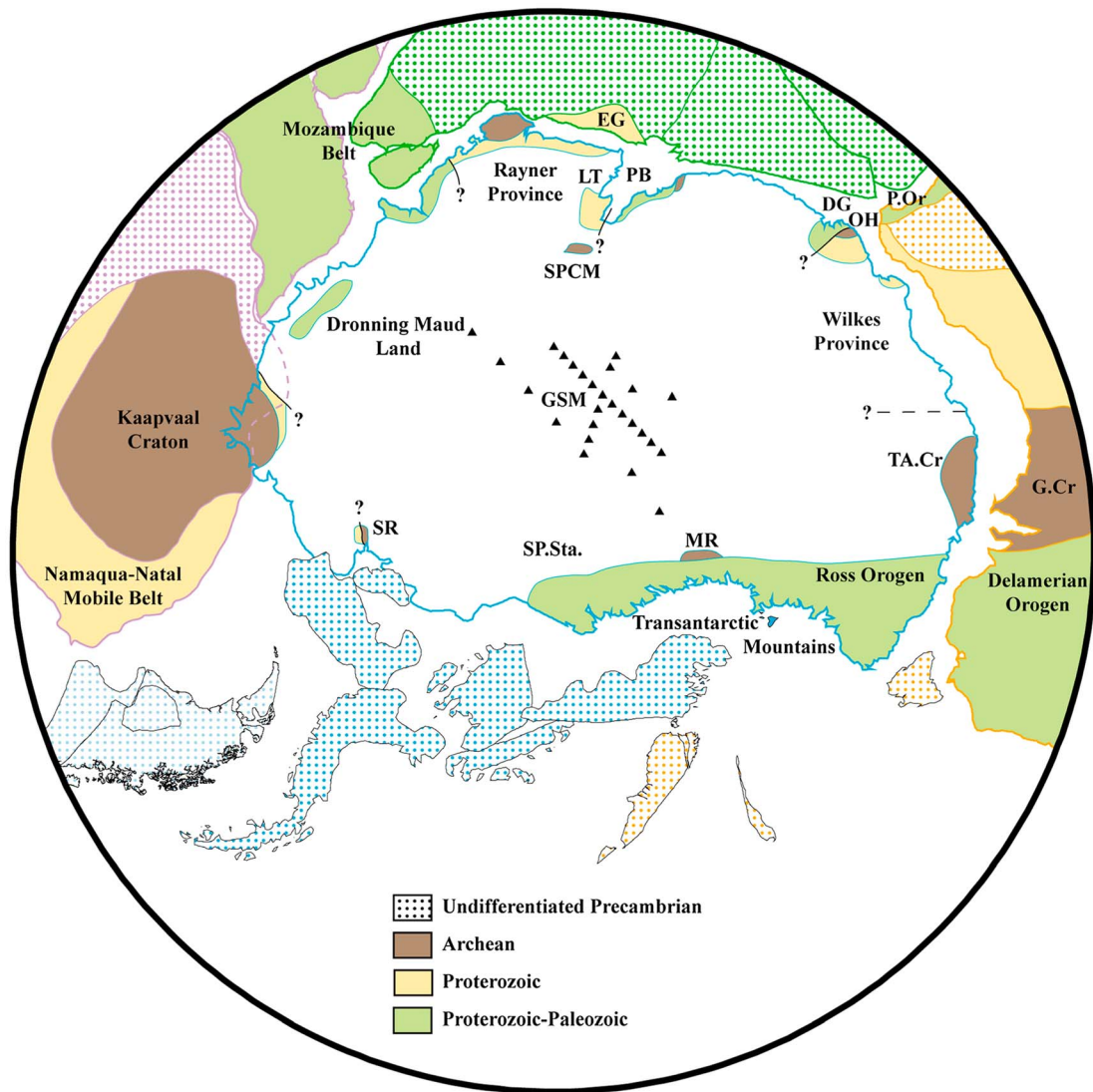
Figure 1. Gondwana reconstruction at 480 Ma, centered on East Antarctica [*Lawver et al.*, 2013], showing the geologic ages of major exposed coastal outcrops [after *Fitzsimons*, 2003]. The black triangles indicate the location of the seismic stations used in this study. Abbreviations are as follows: SR, Shackleton Range; SPCM, Southern Prince Charles Mountains; LT, Lambert Terrane; EG, Eastern Ghats; PB, Prydz Bay; DG, Denman Glacier; OH, Obruchev Hills; P.Or, Pinjarra Orogeny; TA.Cr, Terre Adélie Craton; G.Cr, Gawler Craton; MR, Miller Range; SP.Sta., South Pole Station; GSM, Gamburtsev Subglacial Mountains.

assembly of East Antarctica was not achieved until the early Paleozoic through a series of Neoproterozoic/early Paleozoic orogenic events [*Zhao et al.*, 1995; *Fitzsimons*, 2000a; *Powell and Pisarevsky*, 2002].

[6] Gondwana reconstructions show a strong correlation between the exposed coastal terranes of East Antarctica and those juxtaposed in Africa, India, and Australia (Figure 1). Regions of intense late Neoproterozoic-Early Cambrian tectonism separate three Grenville age provinces that dominate the exposed coastal terranes [*Fitzsimons*, 2000a, 2000b].

In particular, 600–500 Ma Pan-African age tectonism evident in the Raur group of Prydz Bay [*Stüwe and Powell*, 1989; *Zhao et al.*, 1995] and Obruchev Hills in the Denman Glacier region [*Fitzsimons*, 2000a] may indicate the inland extension of the Australian Pinjarra Orogeny into East Antarctica between the Rayner and Wilkes provinces. *Fitzsimons* [2003] suggests that (1) the Australian Pinjarra Orogeny cuts across East Antarctica through the GSM intersecting the Mozambique Belt in the Shackleton Range or (2) intersects the Ross-Delamerian Orogen in the TAM. Alternatively, *Boger et al.* [2001] suggests that (3) this orogeny trends westward through the Lambert

Terrane intersecting the Mozambique Belt somewhere in Dronning Maud Land, and a more recent reinterpretation by *Boger* [2011] further suggests that Mesoproterozoic collisional belt may extend inland from the Denman Glacier region through the Vostok Subglacial Highlands (VSH) to the Shackleton Range.

2.2. Lithospheric Structure of East Antarctica

[7] Global and continental-scale surface wave studies of East Antarctica possessing lateral resolution no better than ~600 km indicate seismically fast upper mantle velocities resembling an old stable Precambrian shield with lithospheric thicknesses of 150 to >250 km [*Roult et al.*, 1994; *Danesi and Morelli*, 2000, 2001; *Ritzwoller et al.*, 2001; *Morelli and Danesi*, 2004; *Kobayashi and Zhao*, 2004]. While some of the lithosphere in East Antarctica may be ≥250 km thick, thinner lithosphere (150–220 km) is suggested beneath the Wilkes Subglacial Basin (WSB) and the Polar Subglacial Basin (PSB), as well as beneath the flanks of the GSM by some models [*Morelli and Danesi*, 2004]. Regional studies indicate that fast upper mantle seismic velocities [*Watson et al.*, 2006; *Lawrence et al.*, 2006a; Heeszel et al., Rayleigh wave constraints on the structure and tectonic history of the Gamburtsev Subglacial Mountains, East Antarctica, submitted to *Journal of Geophysical Research*, 2012, hereafter Heeszel et al., submitted manuscript, 2012] and a region of low attenuation [*Lawrence et al.*, 2006b] extend across much of East Antarctica, consistent with a Precambrian shield.

[8] Surface wave and gravity studies indicate that East Antarctica has a mean crustal thickness of 37–45 km [e.g., *Danesi and Morelli*, 2000; *Ritzwoller et al.*, 2001] and gravity studies further suggest a region of thickened crust (42–63 km) beneath the GSM [*Groushinsky and Sazhina*, 1982a, 1982b; *von Frese et al.* 1999; *Block et al.*, 2009; *Ferraccioli et al.*, 2011]. Recent *S* wave receiver functions (SRFs) [*Hansen*, 2009 and *Hansen et al.*, 2010] and Monte Carlo modeling of shear wave velocities (Heeszel et al., submitted manuscript, 2012) indicate crustal thicknesses of 55–58 km beneath the GSM and 40–45 km beneath the surrounding regions. However, one notable exception is that significantly thinner crust (30–35 km) is observed beneath GM01 (Figure 2) [*Hansen et al.*, 2010; Heeszel et al., submitted manuscript, 2012], AGO1 (Figure 2) (Heeszel et al., submitted manuscript, 2012), and South Pole Station (34 km) [*Baranov*, 2011], reflecting the transition from the East Antarctic Highlands to the PSB.

3. Data and Methodology

3.1. Seismic Data

[9] This study utilizes data collected during the GAMSEIS broadband deployment (Figure 2) in conjunction with the 2007–2008 International Polar Year,
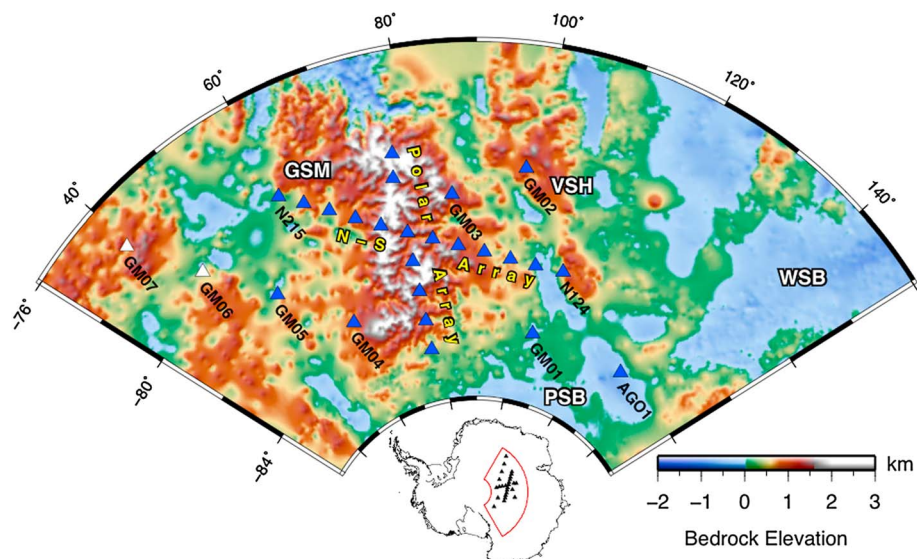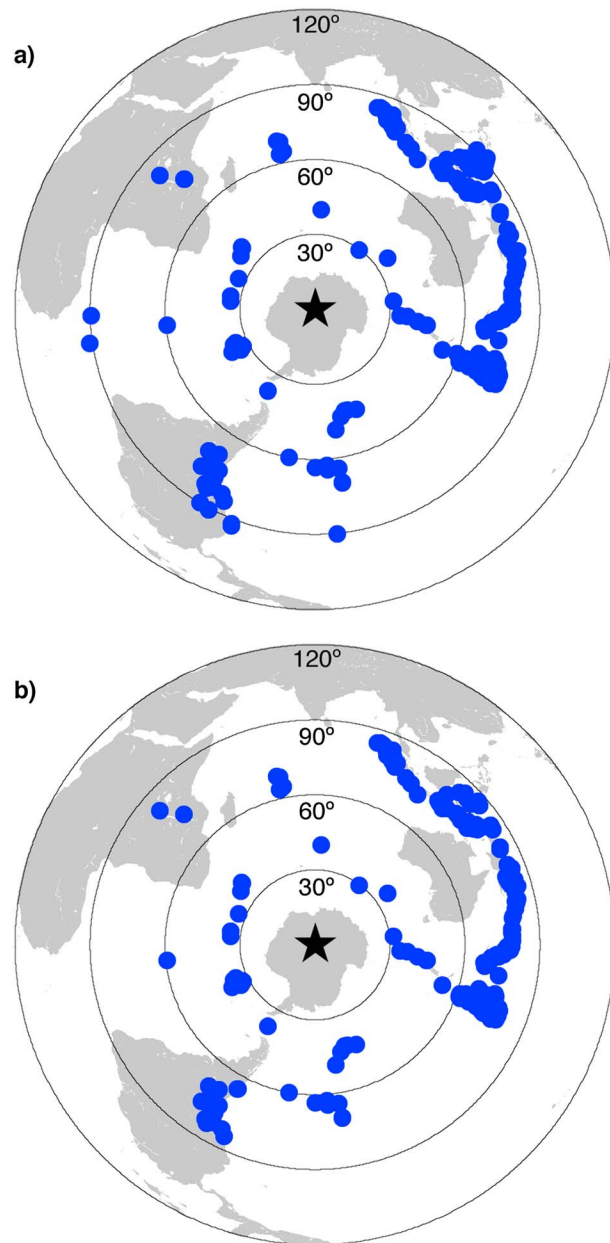

Figure 2. Map of the GAMSEIS seismic array, overlain on bedrock topography from BEDMAP 2 [*Fretwell et al.*, 2012]. The blue and white triangles indicate the location of seismic stations provided by the United States and Japan, respectively. Abbreviations are as follows: GSM, Gamburtsev Subglacial Mountains; VSH, Vostock Subglacial Highlands; PSB, Polar Subglacial Basin; WSB, Wilkes Subglacial Basin.

Antarctica's Gamburtsev Provence (AGAP) project, which also consisted of an aerial geophysical survey (GAMBIT) [*Bell et al.*, 2011; *Ferraccioli et al.*, 2011]. Deployment of the GAMSEIS stations occurred during the 2007–2008 and 2008–2009 Antarctic field season via Twin Otter flights out of South Pole Station and AGAP-S field camp. The bulk of the GAMSEIS array was demobilized during the 2009–2010 Antarctic field season; however, eight

stations remain in operation until at least 2014. The complete GAMSEIS deployment consisted of 26 broadband seismic stations. Twelve stations were arranged in a 900 km long linear array as a continuation of the TAMSEIS N-S array and included the reoccupation of the TAMSEIS stations N124 and N132 [*Watson et al.*, 2006; *Lawrence et al.*, 2006a]. Six stations were arranged in a second 550 km long linear array (Polar array) intersecting the first array and eight stations were installed between the two linear arrays to improve 3-D resolution (Figure 2).

[10] Each station consisted of three main components: (1) either a Guralp 3T or a Nanometrics T240 broadband seismometer installed beneath the snow on a phenolic block and covered by a foam "hat" and plastic dome, (2) a buried insulated box containing a Quanterra Q330 digitizer, hard disk, power module, lithium battery packs, and rechargeable batteries, and (3) a metal pole supporting three 20 W solar panels and a GPS antenna. The GAMSEIS stations operated year-round running on solar power during the austral summer and on lithium battery packs during the austral winter. Stations equipped with a Xeos iridium modem transmitted a daily "state of health" report; however, bandwidth and power limitations prohibited the acquisition of real time data. Despite the extreme conditions, a data return of 87% and 91% was achieved during 2008 and 2009, respectively.

3.2. Relative Arrival Times

[11] Relative arrival times have been determined using the multichannel cross-correlation (MCCC) technique of *VanDecar and Crosson* [1990] on teleseismic *P* and *S* phases from events with $M_w \geq 5.5$ and at distances of 30°–90° and 30°–85°, respectively (Figure 3), in the Fast Archive Recovery Method (FARM) earthquake catalog. The majority of the events are located in the southwest Pacific following the Pacific-Indian plate boundary from Tonga/Fiji to Sumatra or clustered along the South American subduction zone. A small gap in the event distribution occurs toward the central Pacific.

[12] Coherent *P* energy observed throughout all seismograms for a single event was picked from the vertical component after applying a 0.4–2.0 Hz band-pass filter. Similarly, coherent *S* energy was picked from the transverse component after applying a 0.04–0.2 Hz band-pass filter. The resulting *P* and *S* data sets consisted of 3891 *P* arrivals from 288 events and 3299 *S* arrivals from 261 events. When absolute arrival times could be identified, the observed *P* or *S* phases arrived earlier

Figure 3. Event distribution used in the (a) *P* wave and (b) *S* wave tomography models. The black star indicates the center of the array, the blue circles indicate the event locations, and the concentric circles mark distances in 30° increments.

than predicted by the IASP91 velocity model [*Kennett and Engdahl*, 1991], after correcting for the ice and crustal thickness.

[13] Multichannel cross-correlation was applied to a windowed portion of the waveforms relative to an initial pick. A window of [−1.0 s, 2.0 s] was applied to *P* phases and a window of [−5.0 s, 10.0 s] was applied to *S* phases. For *n* traces, the MCCC compares the *i*th trace to the *j*th trace and determines the needed time shift (τ_{ij}) relative to the *i*th pick to achieve the

cross-correlation maximum, resulting in a series of linear equations. To further constrain the system the sum of all relative arrival times for a given event was forced to equal 0.0 s:

$$\left.\begin{array}{l} T_{Ri} - T_{Rj} = \tau_{ij} \\ \sum_{i=1}^{N} T_{Ri} = 0 \end{array}\right\} \Rightarrow \Psi T_R = \tau, \quad (1)$$

where *N* is the number of observations for a given event, T_{Ri} and T_{Rj} are the relative arrival time of the
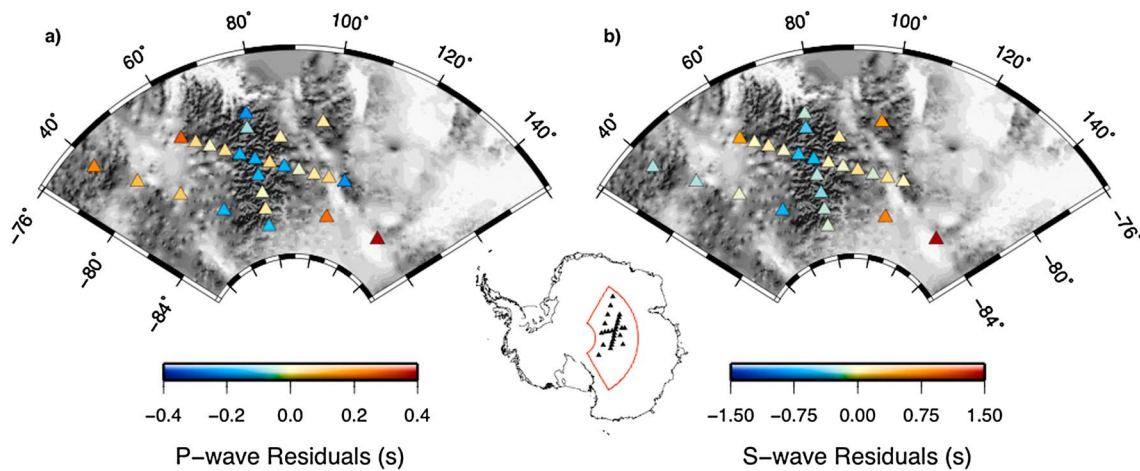

Figure 4. Map of the GAMSEIS array in which the colored triangles indicate the average relative travel time residual for the (a) *P* and (b) *S* data sets. The bedrock topography is also shown in which darker colors indicate higher topography [*Fretwell et al.*, 2012].
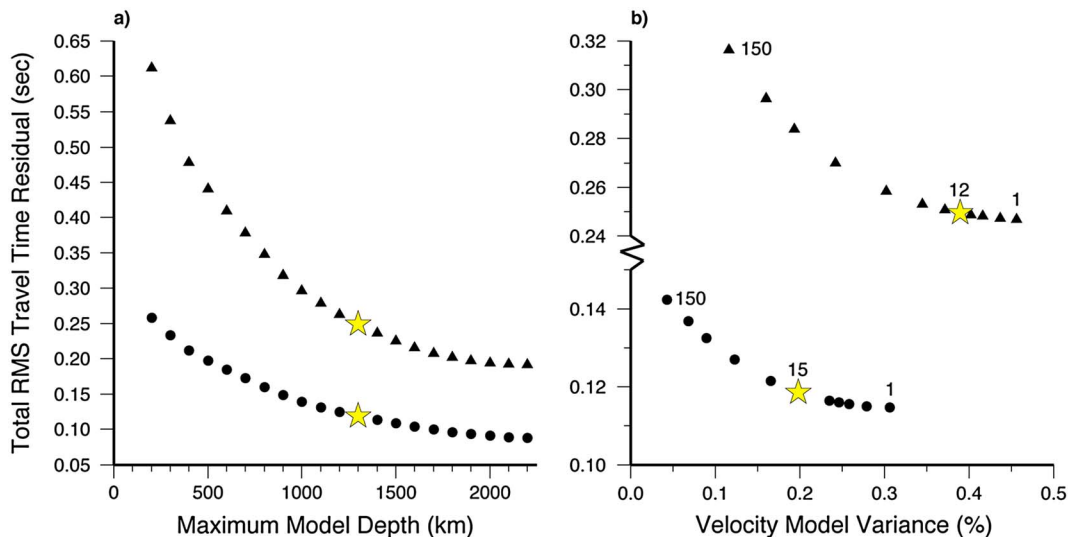
Figure 5. (a) Trade-off curve between the RMS travel time residual and the maximum model depth for both the *P* wave tomography model (circles) and *S* wave tomography model (triangles). The yellow star represents the preferred solution. Damping (*P/S*: 15/12), horizontal smoothing (*P/S*: 0.0008/0.0008), and vertical smoothing (*P/S*: 0.003/0.0008) coefficients were kept fixed during these inversions. (b) Trade-off curve between the RMS travel time residual and the model variance used to choose the optimal damping coefficient. Maximum model depth (1300 km), horizontal smoothing, and vertical smoothing were kept fixed during these inversions.
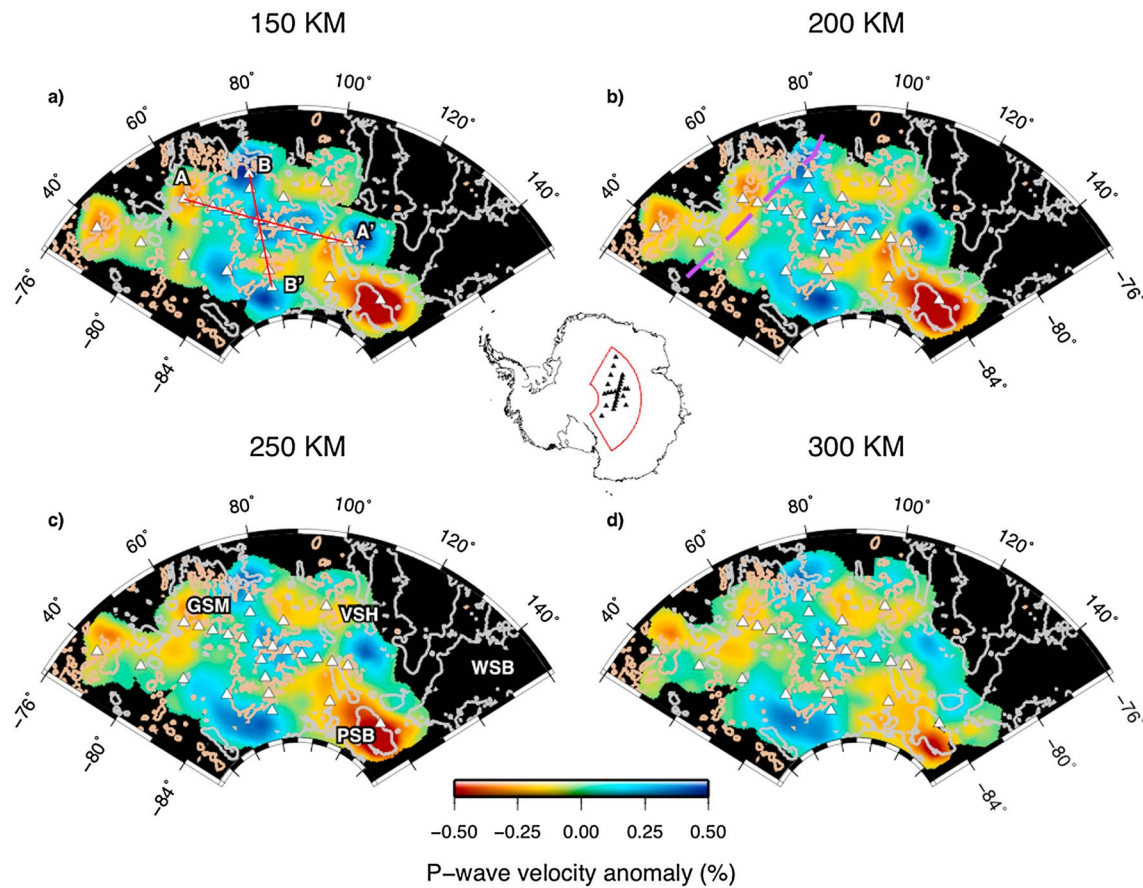
Figure 6. Horizontal slices through the *P* wave tomography model at depths of 150, 200, 250, and 300 km. Each slice shows the 0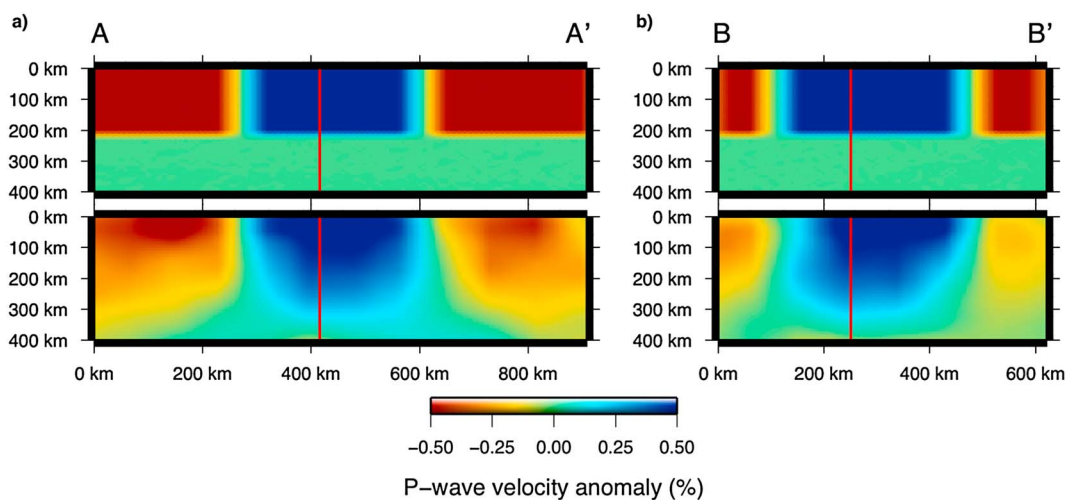 m (gray) and 1000 m (tan) contour from BEDMAP 2 [*Fretwell et al.*, 2012]. The locations of profiles A-A′ and B-B′ are shown in Figure 6a. The purple dashed line in Figure 6b indicates the Gamburtsev suture inferred from aeromagnetic data [*Ferraccioli et al.*, 2011]. Abbreviations are as follows: GSM, Gamburtsev Subglacial Mountains; VSH, Vostok Subglacial Highlands; PSB, Polar Subglacial Basin; WSB, Wilkes Subglacial Basin.
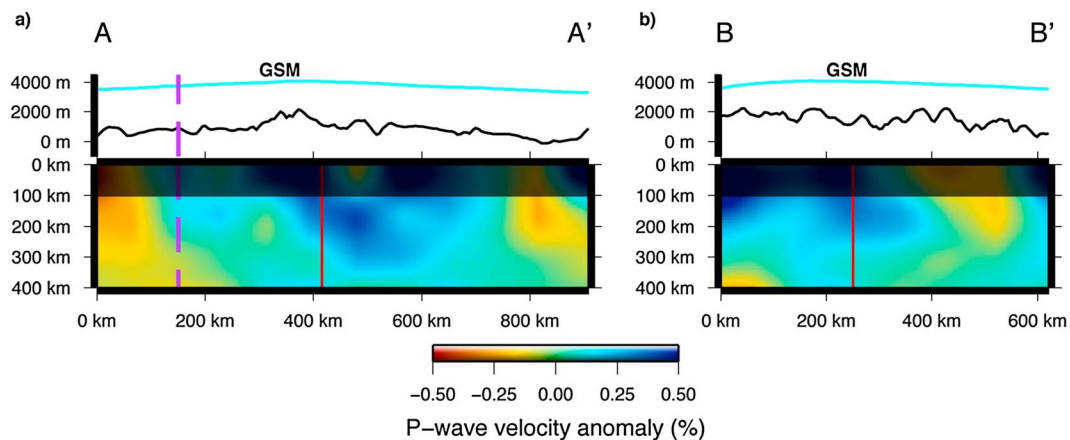
Figure 7. Vertical slices through the *P* wave tomography model along profiles (a) A-A′ and (b) B-B′ (Figure 6a). The red line indicates the intersection of these two profiles. The purple dashed line in Figure 7a is the location of Gamburtsev suture inferred from aeromagnetic data [*Ferraccioli et al.*, 2011]. On the top portion of each figure the black and cyan lines show the bedrock and ice topography from BEDMAP 2, respectively [*Fretwell et al.*, 2012].
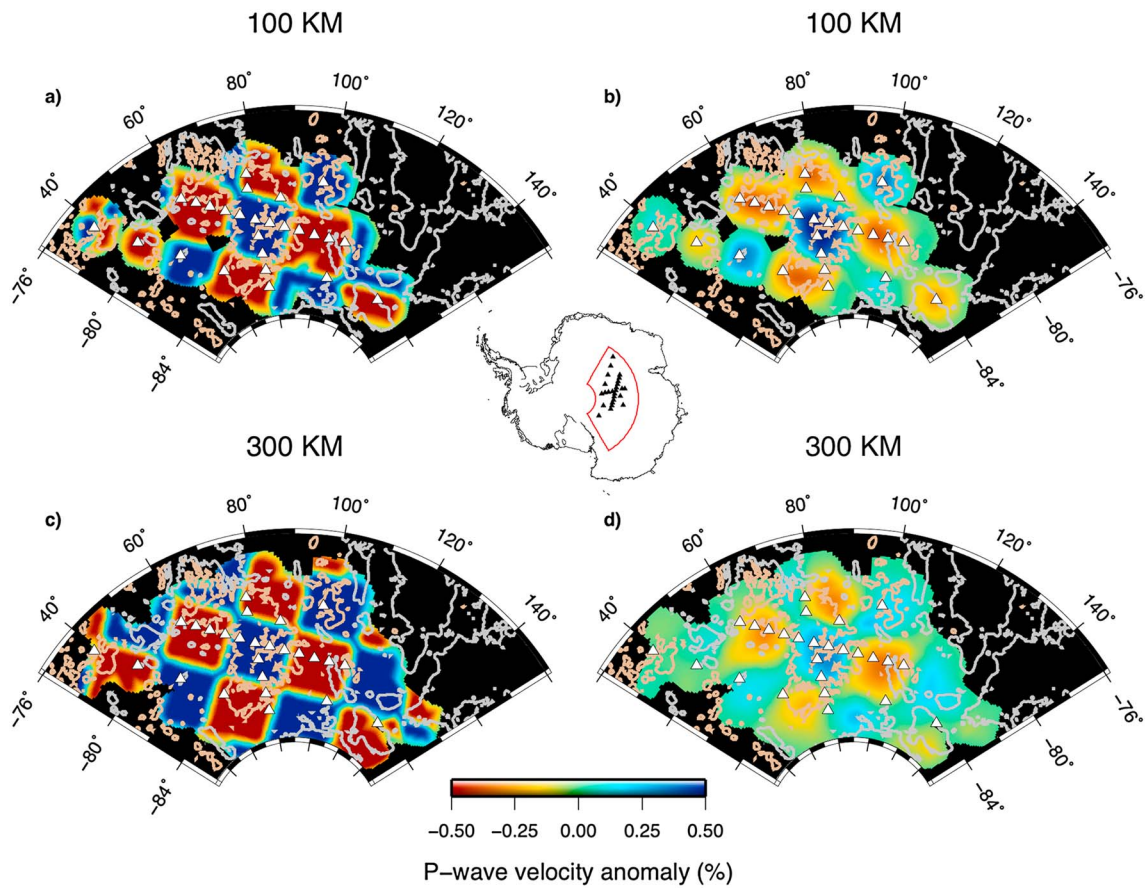
Figure 8. Horizontal slices from the *P* wave resolution tests centered at (a and b) 100 and (c and d) 300 km depths, consisting of ±0.5% checkers that have lateral dimensions of ∼250 × ∼250 km and a thickness of 200 km. Input models are shown on the left and recovered models are on the right.

Figure 9. Profile (a) A-A′ and (b) B-B′ from the *P* wave resolution test, centered at 100 km depth consisting of ±0.5% checkers that have lateral dimensions of ∼250 × ∼250 km and a thickness of 200 km. In each panel, the upper plot is the input model and the lower plot is the recovered model. The red line indicates the intersection of profiles A-A′ and B-B′.
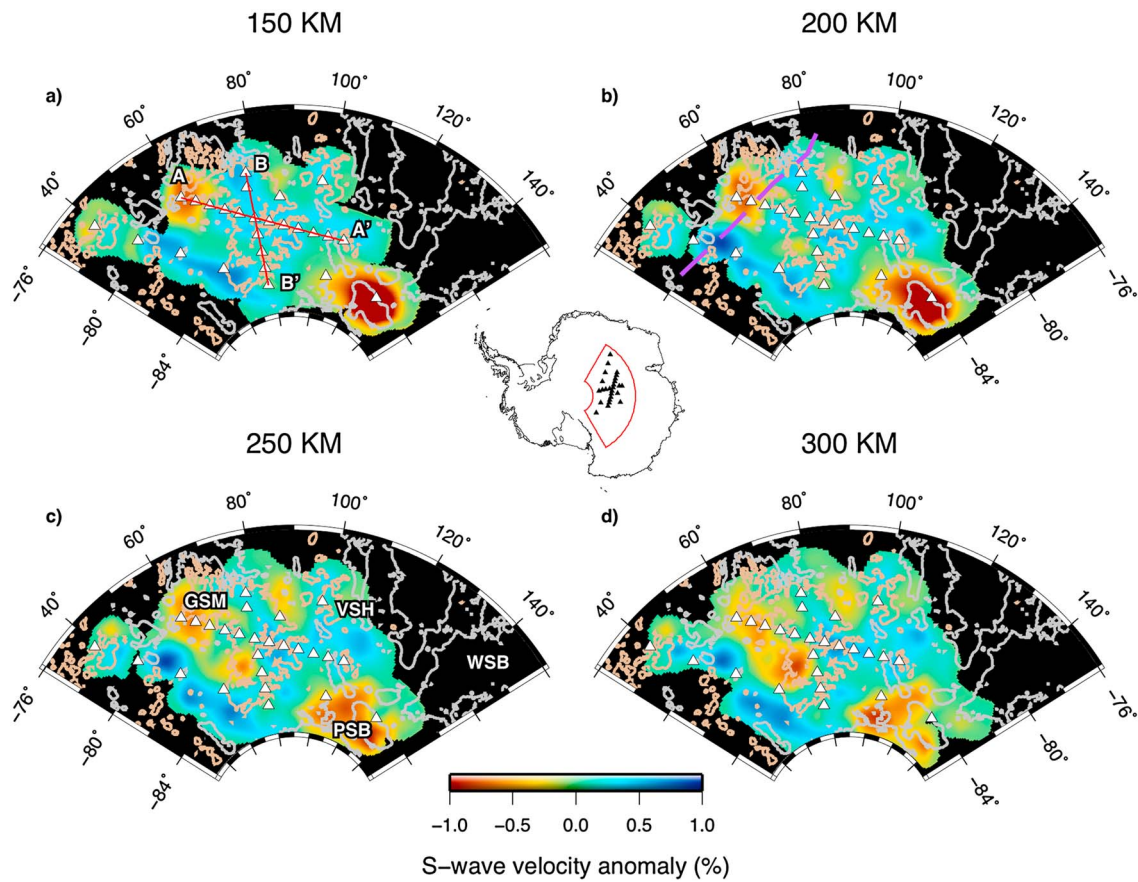
Figure 10. Horizontal slices through the *S* wave tomography model at depths of 150, 200, 250, and 300 km. Each slice shows the 0 m (gray) and 1000 m (tan) contour from BEDMAP 2 [*Fretwell et al.*, 2012]. (a) The locations of profiles A-A′ and B-B′. (b) The Gamburtsev suture inferred from aeromagnetic data in purple dashed line [*Ferraccioli et al.*, 2011]. Abbreviations are as follows: GSM, Gamburtsev Subglacial Mountains; VSH, Vostok Subglacial Highlands; PSB, Polar Subglacial Basin; WSB, Wilkes Subglacial Basin; TAM, Transantarctic Mountains.

Figure 11. Vertical slices through the *S* wave tomography model along profiles (a) A-A′ and (b) B-B′ (Figure 10a). The red line indicates the intersection of these two profiles. The purple dashed line in Figure 11a is the location of Gamburtsev suture inferred from aeromagnetic data [*Ferraccioli et al.*, 2011]. On the top portion of each figure, the black and cyan lines show the bedrock and ice topography from BEDMAP 2, respectively [*Fretwell et al.*, 2012].

9
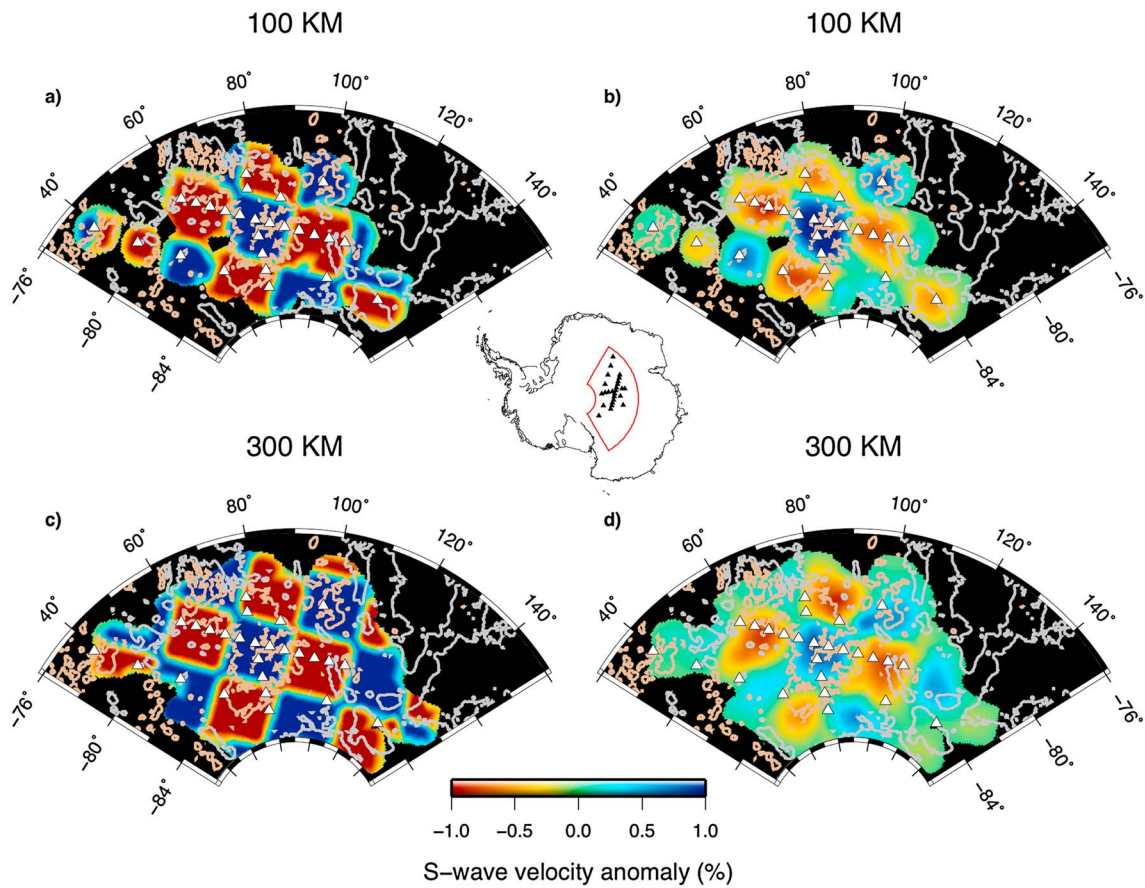
Figure 12. Horizontal slices from the *P* wave resolution tests centered at (a and b) 100 and (c and d) 300 km depths, consisting of ±0.5% checkers that have lateral dimensions of ~250 × ~250 km and a thickness of 200 km. Input models are shown on the left and recovered models are on the right.
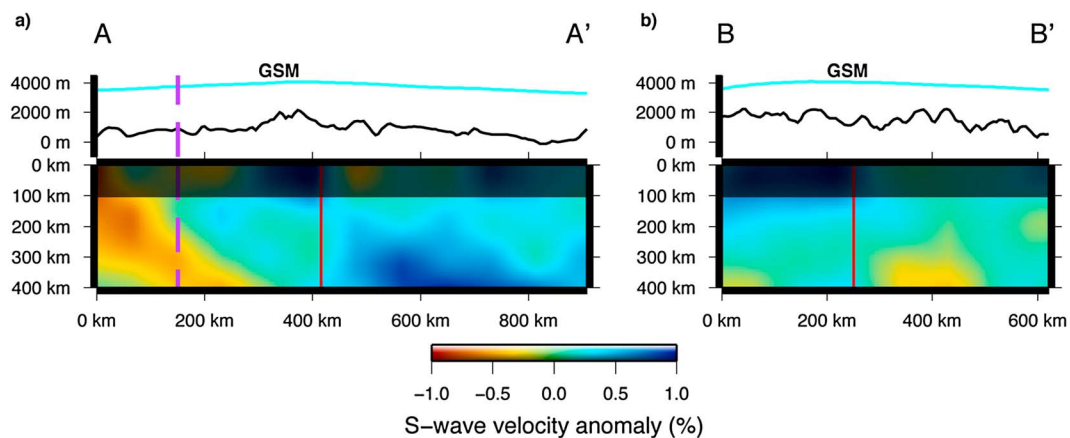

Figure 13. Profile (a) A-A′ and (b) B-B′ from the *P* wave resolution test, centered at 100 km depth consisting of ±0.5% checkers that have lateral dimensions of ~250 × ~250 km and a thickness of 200 km. In each panel, the upper plot is the input model and the lower plot is the recovered model. The red line indicates the intersection of profiles A-A′ and B-B′.
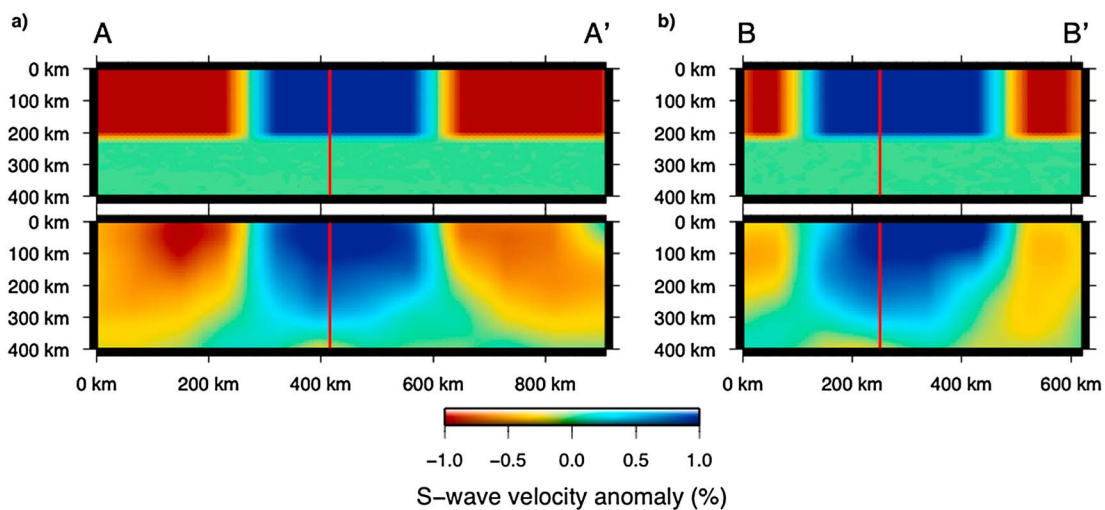
*i*th and *j*th trace, respectively, $\mathbf{\Psi}$ is a $[2 * (N-1)!] \times N$ matrix with entries of ± 1 and 0, $\mathbf{T_R}$ is a vector of relative arrival times, and $\boldsymbol{\tau}$ is a vector containing the

time shifts (τ_{ij}) and the sum of all the relative arrival times for a given event (0.0 s). A linear least squares method was used to solve for the relative arrival times
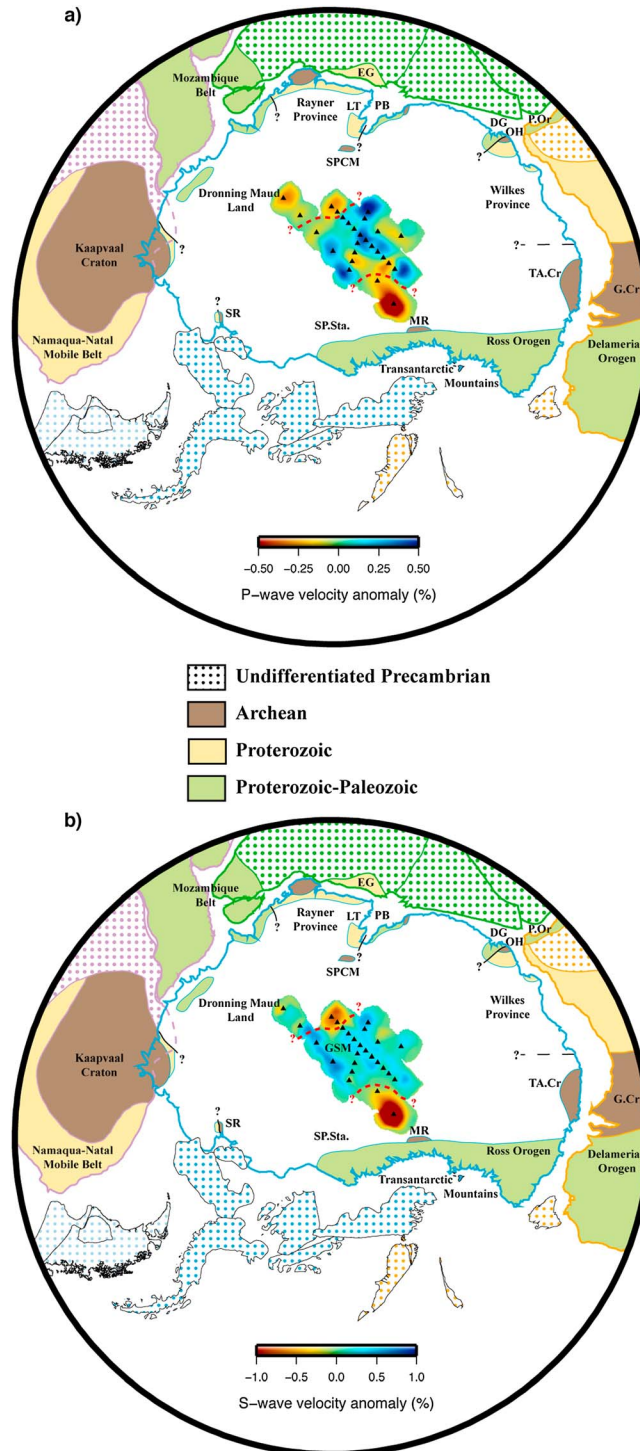
Figure 14. Gondwana reconstruction as was shown in Figure 1 with the 150 km depth slice from the (a) *P* and (b) *S* wave velocity models. The red dashed line indicates lithospheric boundaries inferred from variations in seismic velocity. Abbreviations are as follows: SR, Shackleton Range; SPCM, Southern Prince Charles Mountains; LT, Lambert Terrane; EG, Eastern Ghats; PB, Prydz Bay; DG, Denman Glacier; OH, Obruchev Hills; P.Or, Pinjarra Orogeny; TA.Cr, Terre Adélie Craton; G.Cr, Gawler Craton; MR, Miller Range; GSM, Gamburtsev Subglacial Mountains.

and the event variance ($\sigma_p^2 = 0.02s^2$, $\sigma_s^2 = 0.12s^2$) [*VanDecar and Crosson*, 1990].

3.3. Relative Travel Time Residuals

[14] Theoretical arrival times were calculated using a version of the IASP91 velocity model [*Kennett and Engdahl*, 1991] corrected for Moho depths determined by SRFs and ice thicknesses obtained from either high frequency *P* wave receiver functions or ice-penetrating radar [*Hansen*, 2009; *Hansen et al.*, 2010]. The corrections were made on a station-by-station basis assuming a mean crustal *P* wave velocity of 6.2 km/s (V_p) and *S* wave velocity of 3.6 km/s (V_s), while the *P* and *S* wave velocities of ice are taken to be 3.8 and 1.9 km/s, respectively. These simplified geologic models of the crust and ice are directly dependent on the delay time of the receiver functions and therefore serve as a high-precision station term that not only accounts for the geometry of the ice and crust, but also heterogeneities existing within these layers.

[15] Theoretical arrival times and observed relative arrival times were used to calculate the relative travel time residuals, which preserve only heterogeneity information proximal to the array using

$$\Delta t_i = T_{Ri} - \left[T_{Ti} - \frac{\sum_{j=1}^{N} T_{Tj}}{N} \right], \quad (2)$$

where Δt_i is the relative travel time residual for the *i*th station, T_{Ti} is the absolute theoretical travel time at the *i*th station, and *N* is the number of observations for a given event. Average *P* and *S* wave relative travel time residuals (Figure 4) indicate delayed arrivals beneath the PSB, while the average residuals at the remaining stations are not far removed from the mean (0.0 s).

3.4. Inversion

[16] Relative travel time residuals were inverted using a modified version of the code developed by *Zhao et al.* [1994]. Prior to inverting for velocity, all station and earthquake locations were rotated such that the N-S array lies along the equator. The model space was then laterally partitioned with nodes laid out in a 0.75° by 0.75° grid and vertically partitioned with a node spacing of 25 km from 0 to 400 km depth and node spacing of 50 km from

400 to 1300 km depth. This maximum depth was chosen after investigating the trade-off between the model depth and total RMS travel time residual (Figure 5a). Likewise, optimal damping (Figure 5b) and smoothing coefficients were determined by investigating a wide range of combinations in search of a solution that minimizes damping, while a second derivative smoothing matrix was used to limit high wave number features in the model.

[17] The method developed by *Zhao et al.* [1994] finds the pierce point at the model boundary for a given event-station pair using a dichromatic approach. The raypath from pierce point to station is iteratively determined following the method of *Zhao et al.* [1992], which uses Snell's law to perturb the raypath at velocity discontinuities and the pseudobending algorithm of *Um and Thurber* [1987] to perturb the raypath in regions of continuous velocity. The pseudobending algorithm iteratively perturbs an initial path estimate in a piecewise fashion in order to minimize the travel time; thereby, the ray equations do not have to be directly solved. Using the calculated ray path, the partial derivatives of the travel times with respect to our modified IASP91 velocity model are calculated and a system of equations relating the relative travel time residuals to the medium parameters is determined following *Aki and Lee* [1976], *Thurber* [1983], and *Zhao* [1991]. The resulting large sparse system of equations is then inverted for a relative node velocity using a LSQR conjugate gradient algorithm [*Paige and Saunders*, 1982] with appropriate damping and smoothing coefficients [*Zhao*, 2001, 2004; *Lei and Zhao*, 2007]. The resulting *P* and *S* wave velocity models reduce the variance of the relative travel time residuals by ~86% and ~90%, respectively.

4. Results

4.1. *P* Wave Results

[18] Horizontal slices through the *P* wave velocity model at depths of 150, 200, 250, and 300 km (Figure 6), as well as vertical slices along profiles A-A′ and B-B′ (Figure 7), reveal a fairly uniform velocity structure beneath the study area consisting of broad, weak anomalies with amplitudes ranging from ±0.5%, relative to the mean of the model. At lithospheric depths, these anomalies correlate well with the major terranes dissecting the region. Faster velocity anomalies (≥0.25%) extend to depths of 350 km beneath the GSM and portions

of the VSH, while velocities beneath the remainder of the VSH are near the mean of the model. Slower velocity anomalies (less than or equal to −0.25%) are observed beneath the PSB and regions west of the GSM. At a depth of 350 km, velocity anomalies across the study region decrease to ±0.25%. Although some smaller features (<150 km across) do exist, they are not well resolved and thus are not used in the interpretation.

4.2. P Wave Resolution Test

[19] The resolution of the model has been evaluated by performing several checkerboard tests, in which synthetic travel times are calculated for a given input model. Gaussian random noise with a mean of 0.0 s and a variance of 0.02 s^2 was added to the synthetic residuals in order to account for the P phase event variance of the MCCC. The synthetic travel times were inverted to determine the level at which the input model can be resolved. Figure 8 shows checkerboard resolution tests consisting of ±0.5% anomalies, with lateral dimension of ~250 × ~250 km and a thickness of 200 km centered at 100 and 300 km depth.

[20] The horizontal checkered structure of the input anomalies is recovered beneath the GAMSEIS array at depths of ~150–350 km, beyond which the extent of the anomalies is increasingly influenced by the divergence of the raypaths relative to the array. Vertical resolution is more limited due to the near-vertical ray paths that cause 200 km thick input anomalies to smear to thicknesses of ~300 km (Figure 9), indicating vertical resolution is greater than 100 km. More complex vertical resolution tests, not shown, indicate there is a possibility that alternating slow/fast vertical velocity patterns could go unresolved. However surface wave studies (Heeszel et al., submitted manuscript, 2012) possessing superior vertical resolution indicate such structures do not exist within the study region. Finally, amplitude recovery is between 60% and 80% beneath the N-S and Polar array, while beneath the off-array stations, amplitude recovery is at most 50%.

4.3. S Wave Results

[21] Horizontal slices through the S wave velocity model at depths of 150, 200, 250, and 300 km (Figure 10), as well as vertical slices along profile A-A′ and B-B′ (Figure 11), reveal anomalies of up to ±1.0%. Within the upper 250 km, lateral variations in S wave velocity are generally consistent with

anomalies observed in the P wave velocity model. For example, there are faster velocities (≥0.25%) beneath the GSM and VSH and slower velocities (less than or equal to −0.5%) beneath the PSB and west of the GSM, which are consistent with the P wave velocity model. At depths greater than 250 km, the P and S wave velocity models begin to show less correlation beneath the GSM, possibly due to a more limited raypath coverage in the S wave velocity model compared to the P wave velocity model. Finally, like the P wave velocity model, some smaller-scale features (<150 km across) exist but are not reliably resolved and thus cannot be interpreted.

4.4. S Wave Resolution Test

[22] Similar resolution tests to those performed for the P wave velocity model were carried out for the S wave velocity model (Figures 12 and 13). Gaussian random noise with a mean of 0.0 s and a variance of 0.12 s^2 was added to the synthetic residuals in order to account for the S phase event variance of the MCCC. Results from checkerboard tests with velocity anomalies of ±1.0% are similar to those of the P wave velocity model, possessing good lateral resolution between ~150 and 350 km depth. Vertical resolution is again more limited with 200 km deep anomalies smearing to ~300–350 km depth. Amplitude recovery along the N-S and Polar array is likewise between 60% and 80% and at off-array stations, where the checkered structure is recovered, at most 50% of the amplitude is recovered.

5. Discussion

[23] The P and S wave velocity models show strong lateral correlation of anomalies within the upper 250 km of the mantle, but P and S wave velocity variations are small ($\delta V_p = 1.0\%$, $\delta V_s = 2.0\%$) and thus at best only first-order structures can be interpreted. These include the faster anomalies beneath the GSM and much of the VSH, as well as the slower velocity anomalies beneath the PSB and west of the GSM.

[24] The S wave velocity model agrees reasonably well with a regional S model obtained from surface wave tomography that incorporates data from the TAMSEIS, GAMSEIS, and POLENET deployments [*Heeszel*, 2011], as well as the surface wave study of Heeszel et al. (submitted manuscript, 2012) that uses only the GAMSEIS data set. In particular, at depths of 150–200 km, all models indicate faster velocities beneath the GSM and slower velocities beneath the

PSB. Both surface wave studies account for azimuthal anisotropy [*Heeszel*, 2011; Heeszel et al., submitted manuscript, 2012], while our models assume an isotropic medium. Given this, small variations in lateral velocity in our models may be, in part, due to changes in anisotropic lithospheric fabrics that often dominated Precambrian shields [*Plomerová et al.*, 2011].

[25] Lateral velocity variations in our models are too small to be well resolved by continental-scale tomographic studies; however, after vertical smearing effects are considered, the depth extent of anomalies is consistent with many other models. Anomalies in both the *P* and *S* wave velocity models extend to depths of ≥350 km, and resolution tests suggest these anomalies have smeared vertically ~100–150 km, indicating that these anomalies extend to depths of around 200–250 km. Fast structure extending to such depths (Figures 7 and 11) suggests a lithospheric thickness of 200–250 km across much of the study region, consistent with other velocity models of East Antarctica [*Roult et al.*, 1994; *Danesi and Morelli*, 2000, 2001; *Ritzwoller et al.*, 2001; *Morelli and Danesi*, 2004; *Kobayashi and Zhao*, 2004; Heeszel et al., submitted manuscript, 2012].

5.1. Implications for the Structure of Central East Antarctica

[26] Tomographic studies of continental shields have demonstrated that Archean and Proterozoic terranes can often be delineated based on lithospheric velocity variations, which are typically attributed to a mixture of thermal and compositional effects. Global comparisons of shear wave velocity within cratonic shields determined by surface wave analyses indicate that Meso- or Neoproterozoic lithosphere is on average 3% slower than Archean lithosphere [*Lebedev and van der Hilst*, 2008; *Lebedev et al.*, 2009]. Perhaps the best example of this dichotomy is observed in southern Africa, where the Archean Kaapvaal and Zimbabwe cratons show faster seismic velocities than the surrounding Proterozoic mobile belts. Body wave tomography models of this region indicate that Archean lithosphere is ~2% for δV_p and ~2.5% for δV_s faster than Proterozoic lithosphere [*Fouch et al.*, 2004]. In the following, we discuss the extent to which the anomalies in Figures 6, 7, 10, and 11 can be used to delineate terrane boundaries within central East Antarctica.

[27] Thinner crust [*Hansen et al.*, 2010; *Baranov*, 2011; Heeszel et al., submitted manuscript, 2012] and lithosphere [*Morelli and Danesi*, 2004], as well as a high magnetic anomaly interpreted as unmodified

Precambrian basement of the Nimrod igneous province [*Finn et al.*, 2006; *Goodge and Finn*, 2010] differentiate the PSB from the surrounding East Antarctic highlands. Beneath this region, the lithosphere in our model is 1.0% for δV_p and 1.7% for δV_s slower than beneath the GSM (Figure 14). Resolution tests indicate that this anomaly could be underestimated by as much as 50% and thus similar in magnitude to globally observed differences in lithospheric velocity beneath Archean and Proterozoic terranes [*Fouch et al.*, 2004; *Lebedev and van der Hilst*, 2008; *Lebedev et al.*, 2009]. Zircon U-Pb ages of glacial clasts recovered in the TAM indicate the presence of ~1.1 Ga igneous crust inboard of the central TAM [*Goodge et al.*, 2010]. If this is so, then slower seismic velocities observed beneath the PSB may reflect, at least in part, thinner lithosphere and a warmer geotherm associated with a younger Proterozoic terrane.

[28] Variations in δV_p (0.50%) and δV_s (1.0%) across the GSM and surrounding regions are too small to be readily attributed to significant variations in lithospheric thickness, even after correcting for the 20% reduction in amplitude observed across the N-S array. The velocity variations are of similar magnitude to those observed within distinct Precambrian lithospheric blocks elsewhere, such as the Kaapvaal and Zimbabwe cratons in southern Africa ($\delta V_p = 0.6\%$, $\delta V_s = 0.8\%$) [*Fouch et al.*, 2004], unmodified Grenvillian lithosphere in North America ($\delta V_p = 0.4\%$, $\delta V_s = 0.6\%$) [*Aktas and Eaton*, 2006], and the São Francisco craton in South America ($\delta V_p = 0.5\%$, $\delta V_s = 0.8\%$) [*Rocha et al.*, 2011]. This suggests that the lithosphere beneath the GSM and surrounding regions is of comparable age, although not necessarily a single unit. The variations in velocity may be accommodated by small differences in temperature, or alternatively by a ~26% difference in olivine wt.% (V_p) and a change in Mg# of ~3 (V_s) [*Lee*, 2003; *Schutt and Lesher*, 2010]. Such compositional variability is observed in xenoliths from the Kaapvaal craton [*Schutt and Lesher*, 2010], indicating that variations in velocity across the GSM and surrounding regions could plausibly result from compositional heterogeneity in the lithosphere.

[29] For example, the velocity change of 0.5% in δV_p and 1.0% in δV_s observed on the western flank of the GSM along the N-S array between stations N198 and N206 at 150 km depth (Figures 6, 7a, 10, and 11a) could be indicative of a suture between two lithospheric blocks with somewhat different compositions, but of similar age (Figure 14). In the *P* wave velocity model, the slower velocity region continues to the

southwest beneath stations GM05, GM06, and GM07. In the *S* wave velocity model, a similar slower velocity region is observed beneath stations GM06 and GM07. In both instances, this velocity pattern correlates well with a change in magnetic fabric [*Ferraccioli et al.*, 2011], lending support to this interpretation (Figures 6, 7a, 10, and 11a).

5.2. Implications for the Uplift of the Gamburstev Subglacial Mountains

[30] Our tomographic images, in conjunction with regional and global surface wave studies of Antarctica [*Roult et al.*, 1994; *Danesi and Morelli*, 2000, 2001; *Ritzwoller et al.*, 2001; *Morelli and Danesi*, 2004; *Kobayashi and Zhao*, 2004; Heeszel et al., submitted manuscript, 2012;], indicate that a cold seismically fast upper mantle underlies the majority of East Antarctica. The average Rayleigh wave phase velocity dispersion curves for the study region are most consistent with Archean or Paleoproterozoic terrains globally (Heeszel et al., submitted manuscript, 2012). Therefore, no evidence is found for a significant thermal anomaly beneath the GSM, precluding the existence of a Cenozoic hotspot as suggested by *Sleep* [2006].

[31] A recent model for the origin of the GSM proposed by *Ferraccioli et al.* [2011] invokes a combination of erosional unloading, Permian and Cretaceous rift flank uplift associated with a postulated East Antarctic rift system, and warming of the crustal root beneath the GSM. In this model, it is assumed that Permian extension and Cretaceous transtension led to the formation of a rift system similar to that of the Cenozoic East African rift system, in which rifting occurred in thinner Proterozoic lithosphere that surrounds thicker Archean lithosphere [*Ritsema et al.*, 1998; *Adams et al.*, 2012]. However, the amplitudes of the *P* and *S* wave velocity variations in our models are not consistent with this supposition and instead indicate little change in lithospheric thickness beneath the GSM and surrounding regions.

[32] In addition, as discussed previously, this region has fast velocities extending to depths of >200 km, indicative of thick Archean/Paleoproterozoic lithosphere. Cold thick lithosphere is rheologically strong and thus significant Phanerozoic extension and concomitant thinning of the lithosphere seem unlikely. Nonetheless, if the thick cratonic lithosphere somehow were rifted in the Permian and/or Cretaceous, then the thermal anomaly caused by destroying the cratonic lithosphere and replacing it with warm asthenosphere would persist to the present. For

conductive heat transfer, assuming instantaneous heating of a semi-infinite half-space, the time (τ') required for a thermal anomaly to propagate a distance *l* is given by

$$\tau' = \frac{l^2}{2.32 * \kappa}, \qquad (3)$$

where κ is the thermal diffusivity [*Turcotte and Schubert*, 2002]. Using a κ of 31.5 km^2/Myr and a lithosphere thickness of 200 km, the minimum time required for a thermal anomaly to reach the surface is on the order of 500 Myr and to fully dissipate ~1 Ga. The fact that thick, cold cratonic lithosphere with high seismic velocities at 150–200 km depth is not observed beneath terrains younger than Paleoproterozoic also suggests that the development of cratonic lithosphere requires times greater than 1 Ga. Therefore, a thermal anomaly associated with lithospheric thinning during a Permian and/or Cretaceous rifting event would likely be present today and be resolved in our tomographic images as a pronounced low velocity anomaly. The absence of a significant low velocity anomaly beneath the location of the proposed East Antarctic rift system indicates that our tomographic images are not consistent with the uplift model proposed by *Ferraccioli et al.* [2011].

[33] While we have shown that the analogy to the East African rift system and the uplift model of *Ferraccioli et al.* [2011] is not consistent with our tomographic images, it is still possible that the observed basins are rift features. If this is so, then our results require extension to have been limited causing only minor modification of the upper mantle or to have been accommodated within the brittle lithosphere, and thus leading to negligible rift flank uplift. A possible analog is the Karoo basin system that formed in response to extensional or transtensional stresses associated with the breakup of Gondwana [*Catuneanu et al.*, 2005]. Similar transtensional stresses have been invoked, in part, to explain the basins in central East Antarctica by *Ferraccioli et al.* [2011]. Many Karoo basins formed along the margin of Archean cratons and there are no pronounced velocity anomalies beneath them [Adams *et al.*, 2012].

[34] In another model for the GSM, uplift is attributed to one or more Proterozoic compressional orogenic events that are likely associated with supercontinent assembly during the Pan-African or Grenville [*Fitzsimons*, 2003; *Veevers and Saeed*, 2008; *Boger*, 2011], and would not necessarily destroy or thermally reset the underlying lithosphere. It is at this time that the crustal root of the GSM likely formed. The

preservation of crustal roots beneath ancient compressional orogenic belts is well documented beneath the Ural Mountains [*Grad et al.*, 2009], as well as portions of the Trans-Hudson orogeny [*Hammer et al.*, 2011]. The combination of a low geotherm and fluid-absent conditions may have hindered the eclogitization and delamination of the crustal root beneath these orogenic belts [*Leech*, 2001] and similar conditions may have led to the preservation of the crustal root beneath the GSM, thus prohibiting post-orogenic extensional collapse.

[35] If the GSM are solely a remnant of an ancient orogenic belt, then erosion within the interior of East Antarctica must have proceeded very slowly in order for significant topography to persist to the present day. This may be possible as analyses of detrital apatites from Eocene sands in the Prydz Bay region indicate average erosion rates of 10–20 m/Myr since 250–500 Ma [*Cox et al.*, 2010], while another study has reported erosion rates to be an order of magnitude less for the last 118 Myr [*Jamieson et al.*, 2005]. These low long-term erosion rates are one to two orders of magnitude less than what is typically expected in high relief terranes (i.e., European Alps) [*Bernet et al.*, 2001], requiring either a dry and arid long-term climate or an unusual glacial regime within the interior of East Antarctica [*Cox et al.*, 2010]. The juxtaposition of East Antarctica and Australia until the late Cretaceous opens the possibility that the dry and arid Australian climate, permitting similar low erosion rates (10^0–10^1 m/Myr) and allowing many geologic features to be preserved for tens to hundred million years [*Gale*, 1992], may have existed within the interior of East Antarctica. For example, the Petermann Ranges in central Australia represents the remnants of a ~550 Ma compressional intraplate orogeny associated with the formation of Gondwana [*Aitken et al.*, 2009]. Although only the stumps of this ancient orogeny remain, reaching elevations of at most 1.2 km with relief on the order of 300 m, it is clear that the preservation of ancient highland landscapes is possible, if not unusual.

[36] In addition to the very slow erosion rates, it is also possible that Carboniferous-Permian events, such as the collision of Gondwana and Laurussia [*Veevers*, 1994] or convergence along the Palaeo-Pacific margin of East Antarctica [*Lisker et al.*, 2003] may have led to crustal shortening and reactivation of preexisting faults, thus rejuvenating the ancestral GSM. Regardless of whether or not there was any reactivation of old faults, the *P* and *S* wave velocity models in this study are consistent with an ancient origin for the GSM in which the small amplitude velocity variations within and surrounding the GSM are caused primarily by compositional variations between lithospheric blocks that may be of similar age.

6. Summary and Conclusions

[37] This study utilizes broadband seismic data collected as part of the GAMSEIS deployment in order to develop both *P* and *S* body wave tomography models. Relative arrival times from teleseismic events were determined using the MCCC technique of *Van Decar and Crosson* [1990], and relative travel time residuals were calculated using a modified version of the IASP91 velocity model that accounts for the geometry and heterogeneity of the ice and crust beneath each station. Relative travel time residuals were inverted using the method of *Zhao et al.* [1994] to obtain both *P* and *S* wave velocity models. Classical checkerboard resolution tests were performed to determine the level of resolution achieved by the models. These tests indicate that anomalies similar in magnitude and scale to those observed in the tomographic images are well resolved.

[38] *P* and *S* wave velocity models exhibit small variation in velocity with a nearly identical distribution of fast and slow anomalies within the upper 200–250 km. These anomalies indicate at least two distinct lithospheric blocks that differentiate the slower and likely Meso- or Neoproterozoic PSB from the faster and likely Archean/Paleoproterozoic East Antarctic highlands. Lithospheric velocity variations beneath the East Antarctic highlands are similar to those observed globally within discrete lithospheric blocks. A transition from faster velocities to slower velocities beneath the western flank of the GSM correlates well with a change in magnetic fabric [*Ferraccioli et al.*, 2011] and can be interpreted as a suture between two lithospheric blocks that maybe of similar age. Although much of the tectonic framework in the interior of East Antarctica is still unknown, these results provide important pinning points within the center of East Antarctica (Figure 14) that future tectonic models must take into account.

[39] The small variations in seismic velocities within and surrounding the GSM are inconsistent with the Cenozoic hotspot model of *Sleep* [2006], and also the presence of an analogous East African rift system within the interior of East Antarctica that was most recently active in the Permian and/or Cretaceous, as proposed in the uplift model of *Ferraccioli et al.* [2011]. Instead our models suggest an ancient origin for the GSM, such as an orogenic event associated with supercontinent assembly during the

Neoproterozoic, followed by very slow erosion of the landscape through the Phanerozoic. Possible rejuvenation of the ancestral GSM may have occurred from the Carboniferous-Permian collision of Gondwana with Laurussia or from convergence along the Paleo-Pacific margin of East Antarctica. Regardless of whether or not additional uplift occurred during the Phanerozoic, the long-lived crustal root and high topography of the GSM are geologically unusual and undoubtedly important for the initiation of the East Antarctic ice sheet.

Acknowledgments

References

Adams A., A. Nyblade, and D. S. Weeraratne (2012), Upper mantle shear wave velocity structure beneath the East African plateau: Evidence for a deep, plateau wide low velocity anomaly, *Geophys. J. Int.*, *189*, 123–142, doi: 10.1111/j.1365-246X.2012.05373.x.

Aitken, A. R. A., P. G. Betts, and L. Ailleres (2009), The architecture, kinematics, and lithospheric processes of a compressional intraplate orogen occurring under Gondwana assembly: The Petermann orogeny, central Australia, *Lithosphere*, *1(6)*, 343–357.

Aki, K. and W. H. K. Lee (1976), Determination of three dimensional velocity anomalies under a seismic array using first P arrival times from local earthquakes 1. A homogeneous initial model, *J. Geophys. Res.*, *81*, 4381–4399.

Aktas, K., and D. W. Eaton (2006), Upper-mantle velocity structure of the lower Great Lakes region, *Tectonophysics*, *420*, 267–281, doi: 10.1016/j.tecto.2006.01.020.

Baranov, A. A. (2011), Moho depth in Antarctica from seismic data, *Phys Solid Earth*, *47*, 1058–1070, doi: 10.1134/S1069351311120019.

Bell, R. E., et al. (2011), Widespread persistent thickening of the East Antarctic Ice Sheet by freezing from the base, *Science*, *331*, 1592–1595, doi: 10.1126/science.1200109.

Bernet, M., M. Zattin, J. I. Garver, M. T. Brandon, and J. A. Vance (2001), Steady-state exhumation of the European Alps, *Geology*, *29*, 35–38.

Block, A. E., R. E. Bell, and M. Studinger (2009), Antarctic crustal thickness from satellite gravity: Implications for

the Transantarctic and Gamburtsev Subglacial Mountains, *Earth Planet. Sci. Lett.*, *288*, 194–203, doi: 10.1016/j.epsl.2009.09.022.

Boger, S. D. (2011), Antarctica—Before and after Gondwana, *Precam. Res.*, *19*, 335–371, doi: 10.1016/j.gr.2010.09.003.

Boger, S. D., C. J. L. Wilson, and C. M. Fanning (2001), Early Paleozoic tectonism within the East Antarctic craton: The final suture between east and west Gondawana?, *Geology*, *29*, 463–466.

Bo, S., M. J. Seigert, S. M. Mudd, D. Sugden, S. Fujita, C. Xianbin, J. Yunyun, T. Xueyuan, and L. Yuansheng (2009), The Gamburtsev mountains and the origin and early evolution of the Antarctic Ice Sheet, *Nature*, *459*, 690–693, doi: 10.1038/nature08024.

Catuneanu, O., H. Wopfner, P. G. Eriksson, B. Cairncross, B. S. Rubidge, R. M. H. Smith, and P. J. Hancox (2005), The Karoo basins of south-central Africa, *J. African Earth Sci.*, *43*, 211–253, doi: 10.1016/j.jafrearsci.2005.07.007.

Cox, S. E., S. N. Thomson, P. W. Reiners, S. R. Hemming, and T. van de Flierdt (2010), Extremely low long-term erosion rates around the Gamburtsev Mountains in interior East Antarctica, *Geophys. Res. Lett.*, *37*, L22307, doi: 10.1029/2010GL045106.

Dalziel, I. W. D. (1991), Pacific margins of Laurentia and East Antarctica-Australia as a conjugate rift pair: Evidence and implications for an Eocambrian supercontinent, *Geology*, *19*, 598–601.

Danesi, S., and A. Morelli (2000), Group velocity of Rayleigh waves in the Antarctic region, *Phys. Earth Planet. Int.*, *122*, 55–66.

Danesi, S., and A. Morelli (2001), Structure of the upper mantle under the Antarctic plate from surface wave tomography, *Geophys. Res. Lett.*, *28*, 4395–4398.

Ferraccioli, F., C. A. Finn, T. A. Jordan, R. E. Bell, L. M. Anderson, and D. Damaske (2011), East Antarctic rifting triggers uplift of the Gamburtsev Mountains, *Nature*, *479*, 388–392, doi: 10.1038/nature10566.

Finn, C. A., J. W. Goodge, D. Damaske, and C. M. Fanning (2006), Scouting craton's edge in Paleoproterozoic Gondwana, in *Antarctica—Contributions to Global Earth Sciences (Proceedings of ISAES IX, Potsdam, 9–12 September 2003)*, edited by D. Dutterer et al., pp. 165–174, Springer, New York.

Fitzsimons, I. C. W. (2000a), Grenville-age basement provinces in East Antarctica: Evidence for three separate collisional orogens, *Geology*, *28*, 879–882.

Fitzsimons, I. C. W. (2000b), A review of tectonic events in the East Antarctic Shield and their implications for Gondwana and earlier supercontinents, *J. African Earth Sci.*, *31*, 3–23.

Fitzsimons, I. C. W. (2003), Proterozoic basement provinces in southern and southwestern Australia, and their correlation with Antarctica, in *Proterozoic East Gondwana: Supercontinent Assembly and Breakup*, edited by M. Yoshida, B. F. Windley and S. Dasgupta, pp. 93–130, Geological Society, London, Special Publication, London.

Fouch, M., D. E. James, J. C. VanDecar, and S. van der Lee (2004), Mantle seismic structure beneath the Kaapvaal and Zimbabwe cratons, *S. African J. of Geology*, *107*, 33–44.

Fretwell, P., et al. (2012), BEDMAP2: Improved ice bed, surface, and thickness datasets for Antarctica, *Cryosphere Discuss.*, *6*, 4305–4361, doi: 10.5194/tcd-6-4305-2012.

Gale, S. (1992), Long-term landscape evolution in Australia, *Earth Surf. Proc. Landforms*, *17*, 323–343.

Goodge, J. W. and C. A. Finn (2010), Glimpses of East Antarctica: Aeromagnetic and satellite magnetic view from the central

Transantarctic Mountains of East Antarctica, *J. Geophys. Res.*, *115*, B09103, doi: 10.1029/2009JB006890.

Goodge, J. W., C. M. Fanning, and V. C. Bennett (2001), U-Pb evidence of ~1.7 Ga crustal tectonism during the Nimrod Orogeny in the Transantarctic Mountains, Antarctica: Implications for Proterozoic plate reconstructions, *Precam. Res.*, *112*, 261–288.

Goodge, J. W., C. M. Fanning, D. M. Brecke, K. J. Licht, and E. F. Palmer (2010), Continuation of the Laurentian Grenville Province across the Ross Sea Margin of East Antarctica, *J. Geology*, *118*, 601–619, doi: 10.1086/656385.

Grad, M., T. Tiira, and ESC Working Group (2009), Moho depth map of the European Plate, *Geophys. J. Int.*, *176*, 279–292, doi: 10.1111/j.1365-246X.2008.03919.

Groushinsky, N. P. and N. B. Sazhina (1982a), Some features of Antarctic crustal structure, *Int. Union Geol. Sci.*, *4*, 907–911.

Groushinsky, N. P. and N. B. Sazhina (1982b), Gravitational field of Antarctica, *Int. Union Geol. Sci.*, *4*, 913–917.

Hammer, P. T. C., R. M. Clowes, F. A. Cook, K. Vasudevan, and A. J. vander Velden (2011), The big picture: A lithospheric cross section of the North American continent, *GSA Today*, *21*, 6, 4–10 doi: 10.1130/GSA TG95A.1

Hansen, S. E., J. Julia, A. A. Nyblade, M. L. Pyle, D. A. Wiens, and S. Anandakrishnan (2009), Using S wave receiver functions to estimate crustal structure beneath ice sheets: An application to the Transantarctic Mountains and East Antarctic craton, *Geochem. Geophys. Geosyst.*, *10*(8), Q08014, doi: 10.1029/2009GC002576.

Hansen, S. E., A. A. Nyblade, D. S. Heeszel, D. A. Wiens, P. J. Shore, and M. Kanao (2010), Crustal structure of the Gamburtsev Mountains, East Antarctica, from S-wave receiver functions and Rayleigh wave phase velocities, *Earth Planet. Sci. Lett.*, *300*, 395–401, doi: 10.1016/j.epsl.2010.10.022.

Heeszel, D. (2011), Surface wave derived shear velocity structure of the Gamburtsev Subglacial Mountains, Transantarctic Mountains and West Antarctica and shallow seismicity of the Mariana and Tonga subduction zones, Ph.D. thesis, Dept. of Earth and Planet. Sci., Washington University in St. Louis, St. Louis, Missouri, United States.

Hoffman, P. F. (1991), Did the breakout of Laurentia turn Gondwanaland inside out?, *Science*, *252*, 1409–1412.

Jamieson, S. S. R., N. R. J. Hulton, D. Sugden, A. J. Payne, and J. Taylor (2005), Cenozoic landscape evolution of the Lambert Basin, East Antarctica: The relative role of rivers and ice sheets, *Global Planet Change*, *45*, 35–49.

Kennett, B. L. N., and E. R. Engdahl (1991), Traveltimes from global earthquake location and phase identification, *Geophys. J. Int.*, *105*, 429–465.

Kobayashi, R., and D. Zhao (2004), Rayleigh wave group velocity distribution in the Antarctic region, *Phys. Earth Planet. Inter.*, *141*, 167–181, doi: 10.1016/jpepi.2003.11.011.

Lawrence, J. F., D. A. Wiens, A. A. Nyblade, S. Anandakrishnan, P. J. Shore, and D. Voight (2006a), Rayleigh wave phase velocity analysis of the Ross Sea, Transantarctic Mountains, and East Antarctica from a temporary seismograph array, *J. Geophys. Res.*, *111*, doi: 10.1029/2005JB003812.

Lawrence, J. F., D. A. Wiens, A. A. Nyblade, S. Anandakrishnan, P. J. Shore, and D. Voight (2006b), Upper mantle thermal variations beneath the Transantarctic Mountains inferred from teleseismic S-wave attenuation, *Geophys. Res. Lett.*, *33*, doi: 10.1029/2005GL024516.

Lawver, L. A., I. W. D. Dalziel, and L. M. Gahagan (2013), Intercontinental migration routes for South American land mammals: Paleogeographic constraints, in *Origins and Evolution of Cenozoic South American Mammals*, edited by A. I. Rosenberger and M. F. Tejedor, Springer, New York, NY, in press.

Lebedev, S., J. Boonen, and J. Trampert (2009), Seismic structure of Precambrian lithosphere: New constraints from broad-band surface-wave dispersion, *Lithos*, *109*, 96–111, doi: 10.1016/j.lithos.2008.06.010.

Lebedev, S., and R. D. van der Hilst (2008), Global upper-mantle tomography with the automated multimode inversion of surface and S-wave forms, *Geophys. J. Int.*, *173*, 505–518, doi: 10.1111/j.1365-246X.2008.03721.x.

Lee, C. A. (2003), Compositional variation of density and seismic velocities in natural peridotites at STP conditions: Implications for seismic imaging of compositional heterogeneities in the upper mantle, *J. Geophys. Res.*, *108*, doi: 10.1029/2003JB002413.

Leech, M. L. (2001), Arrested orogenic development: Eclogitization, delamination, and tectonic collapse, *Earth Planet. Sci. Lett.*, *185*, 149–159.

Lei, J. and D. Zhao (2007), Teleseismic P-wave tomography and the upper mantle structure of the central Tien Shan orogenic belt, *Phys. Earth Planet. Int.*, *162*, 165–185.

Lisker, F., R. Brown, and D. Fabel (2003), Denudational and thermal history along a transect across the Lambert Graben, northern Prince Charles Mountains, Antarctica, derived from apatite fission track thermochronology, *Tectonics*, *22*(5), doi: 10.1029/2002TC001477.

Moores, E. M. (1991), Southwest-U.S.-East Antarctic (SWEAT) connection: A hypothesis, *Geology*, *19*, 425–428.

Morelli, A., and S. Danesi (2004), Seismological imaging of the Antarctic continental lithosphere: A review, *Global Planet Change*, *42*, 155–165, doi: 10.1016/j.gloplacha.2003.12.005.

Paige C. C. and M. A. Saunders (1982), LSQR: An algorithm for sparse linear equations and sparse least squares, *ACM Trans. Math. Software*, *8*, 1, 43–71.

Phillips, G., and A. L. Läufer (2009), Brittle deformation relating to the Carboniferous-Cretaceous evolution of the Lambert Graben, East Antarctica: A precursor for Cenozoic relief development in an intraplate and glaciated region, *Tectonophysics*, *471*, 216–224, doi: 10.1016/j.tecto.2009.02.012.

Plomerová, J., L. Vecsey, and LAPNET Working Group (2011), Domains of Archean mantle lithosphere deciphered by seismic anisotropy—Inferences from the LAPNET array in northern Fennoscandia, *Solid Earth*, *2*, 303–313, doi: 10.5194/se-2-303-2011.

Powell, C. M. A., and S. A. Pisarevsky (2002), Late Neoproterozoic assembly of East Gondwana, *Geology*, *30*, 3–6.

Ritsema, J., A. A. Nyblade, T. J. Owens, C. A. Langston, and J. C. VanDecar (1998), Upper mantle seismic velocity structure beneath Tanzania, east Africa: Implications for the stability of cratonic lithosphere, *J. Geophys. Res.*, *103*, 21201–21213.

Ritzwoller, M. H., N. M. Shapiro, A. L. Levshin, and G. M. Leahy (2001), Crustal and upper mantle structure beneath Antarctica and surrounding oceans, *J. Geophys. Res.*, *106*(12), 30645–30670.

Rocha, M. P., M. Schimmel, and M. Assumpção (2011), Upper-mantle seismic structure beneath SE and Central Brazil from P- and S-wave regional traveltime tomography, *Geophys. J. Int.*, *184*, 268–286, doi: 10.1111/j.1365-246X2010.04831.x.

Rogers, J. J., R. Unrug, and M. Sultan (1995), Tectonic assembly of Gondwana, *J. Geodyn.*, *19*, 1–34.

Roult, G., D. Rouland, and J. P. Montagner (1994), Antarctica II: Upper mantle structure from velocities and anisotropy, *Phys. Earth Planet. Int.*, *84*, 33–57.

Schutt, D. L., and C. E. Lesher (2010), Compositional trends among Kaapvaal Craton garnet peridotite xenoliths and their effects on seismic velocity and density, *Earth Planet. Sci. lett. 300*, 367–373, doi: 10.1016/j.epsl.2010.10.018.

Sleep, N. H. (2006), Mantle plumes from top to bottom, *Earth. Sci. Rev.*, *77*, 231–271, doi: 10.1016/j.earscirev.2006.03.007.

Stüwe, K., and R. Powell (1989), Low-pressure granulite facies metamorphism in the Larsemann Hills area, East Antarctica: Petrology and tectonic implications for the evolution of the Prydz Bay area, *J. Metamorphic Geol.*, *7*, 465–483.

Thurber, C. H. (1983), Earthquake locations and three-dimensional crustal structure in the Coyote Lake Area, Central California, *J. Geophys. Res.*, *88*, B10, 8226–8236.

Tingey, R. J. (1991), The regional geology of Archaean and Proterozoic rocks in Antarctica, in *The Geology of Antarctica*, edited by R. J. Tingey, pp. 1–73, Oxford University Press, Oxford, U.K.

Turcotte, D. L. and G. Schubert (2002), *Geodynamics*, 2nd Edition, Cambridge University Press, New York, NY.

Um, J., and C. H. Thurber (1987), A fast algorithm for two-point seismic ray tracing, *Bull. Seismol. Soc. Am.*, *77*, 972–986

VanDecar, J. C., and R. S. Crosson (1990), Determination of teleseismic relative phase arrival times using multi-channel cross-correlation and least squares, *Bull. Seismol. Soc. Am.*, *80*, 150–169.

van de Flierdt, T., S. R. Hemming, S. L. Goldstein, G. E. Gehrels, and S. E. Cox (2008), Evidence against a young volcanic origin of the Gamburtsev Subglacial Mountains, Antarctica, *Geophys. Res. Lett.*, *35*, L21303, doi: 10.1029/2008GL035564.

Veevers, J. J. (1994), Case for the Gamburtsev Subglacial Mountains of East Antarctica originating by mid-Carboniferous shortening of an intracratonic basin, *Geology*, *22*, 593–596.

Veevers, J. J., and A. Saeed (2008), Gamburtsev Subglacial Mountains provenance of Permian-Triassic sandstones in the Prince Charles Mountains and offshore Prydz Bay: Integrated U-Pb and TDM ages and host-rock affinity from detrital zircons, *Gondwana Res.*, *14*, 316–342, doi: 10.1016/j.gr.2007.12.007.

Veevers, J. J., and A. Saeed (2011), Age and composition of Antarctic bedrock reflected by detrital zircons, erratics, and recycled microfossils in the Prydz Bay-Wilkes Land-Ross Sea-Marie Byrd Land sector (70°–240°E), *Gondwana Res.*, doi: 10.1016/j.gr.2011.03.007.

von Frese, R. R. B., L. Tan, J. W. Kim, and C. R. Bently (1999), Antarctic crustal modeling from the spectral correlation of free-air gravity anomalies with the terrain, *J. Geophys. Res.*, *104(*B11*)*, 25, 275–225.

Watson, T., A. Nyblade, D. A. Wiens, S. Anandakrishnan, M. Benoit, P. J. Shore, D. Voigt, J. VanDecar (2006), P and S velocity structure of the upper mantle beneath the Transantarctic Mountains, East Antarctic craton, and Ross Sea from travel time tomography, *Geochem. Geophys. Geosyst.*, *7*, Q07005, doi: 10.1029/2005GC001238.

Wessel, P., and W. H. F. Smith (1998), New, improved version of Generic Mapping Tools released, *Eos. Trans. AGU*, *79(*47*)*.

Zhao, D. (1991), A tomographic study of seismic velocity structure in the Japan Islands, Ph.D. thesis, Dept. of Geophys., 301 pp., Tohoku Univ., Sendai, Japan.

Zhao, D. (2001), Seismic structure and origin of hotspots and mantle plumes, *Earth Planet. Sci. Lett.*, *192*, 251–265.

Zhao, D. (2004), Global tomographic images of mantle plumes and sub-ducting slabs: Insight into deep Earth dynamics, *Phys. Earth Planet. Int.*, *146*, 3–34.

Zhao D., A. Hasegawa, and H. Kanamori (1994), Deep structure of Japan subduction zone as derived from local, regional, and teleseismic events, *J. Geophys. Res.*, *99*, B11, 22,313–22,329.

Zhao D., A. Hasegawa, and S. Huriuchi (1992). Tomographic imaging of P and S wave velocity structure beneath northeastern Japan, *J. Geophys. Res.*, *97*, B13, 19,909–19,928.

Zhao, Y., X. Liu, B. Song, Z. Zhang, J. Li, Y. Yao and Y. Wang (1995), Constraints on the stratigraphic age of metasedimentary rocks from the Lasermann Hills, E. Antarctica: Possible implications for Neoproterozoic tectonics, *Precam. Res.*, *75*, 175–188.